









RESEARCH ARTICLE | FEBRUARY 07 2025

# Vortex-driven nanogenerators for marine energy harvesting and flow velocity sensing

Special Collection: [Recent Advances in Fluid Dynamics and Its Applications](#)Peng Xu (徐鹏) ; Mingjie Hong (洪铭杰) ; He Li (李贺) ; Chenlu Song (宋忱潞)  ; Ould el Moctar ; Changqing Jiang (蒋长青)  *Physics of Fluids* 37, 027133 (2025)<https://doi.org/10.1063/5.0250873>

## Articles You May Be Interested In

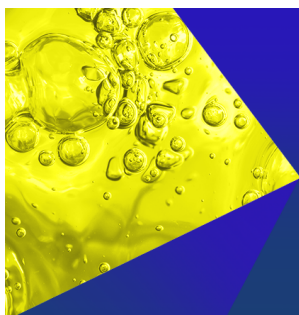
Harvest of ocean energy by triboelectric generator technology

*Appl. Phys. Rev.* (August 2018)

PVC/MXene electrospun film triboelectric nanogenerator for efficient mechanical energy harvesting and multifunctional human motion sensing

*APL Mater.* (January 2025)

Honeycomb-like nanofiber based triboelectric nanogenerator using self-assembled electrospun poly(vinylidene fluoride-co-trifluoroethylene) nanofibers

*Appl. Phys. Lett.* (April 2016)

Physics of Fluids  
Special Topics  
Open for Submissions

[Learn More](#)



# Vortex-driven nanogenerators for marine energy harvesting and flow velocity sensing

Cite as: Phys. Fluids **37**, 027133 (2025); doi: [10.1063/5.0250873](https://doi.org/10.1063/5.0250873)

Submitted: 27 November 2024 · Accepted: 14 January 2025 ·

Published Online: 7 February 2025



View Online



Export Citation



CrossMark

Peng Xu (徐鹏),<sup>1,2</sup> Mingjie Hong (洪铭杰),<sup>1</sup> He Li (李贺),<sup>1</sup> Chenlu Song (宋忱璐),<sup>3,a)</sup> Ould el Moctar,<sup>4</sup> and Changqing Jiang (蒋长青)<sup>4,a)</sup>

## AFFILIATIONS

<sup>1</sup>School of Naval Architecture and Maritime, Zhejiang Ocean University, Zhoushan 316022, China

<sup>2</sup>State Key Laboratory of Ocean Engineering, Shanghai Jiao Tong University, Shanghai 20024, China

<sup>3</sup>School of Marine Engineering Equipment, Zhejiang Ocean University, Zhoushan 316022, China

<sup>4</sup>Institute of Sustainable and Autonomous Maritime Systems, University of Duisburg-Essen, Duisburg 47057, Germany

**Note:** This paper is part of the Special Topic, Recent Advances in Fluid Dynamics and Its Applications.

<sup>a)</sup>Authors to whom correspondence should be addressed: [songchenlu@zjou.edu.cn](mailto:songchenlu@zjou.edu.cn) and [changqing.jiang@uni-due.de](mailto:changqing.jiang@uni-due.de)

## ABSTRACT

With the growing focus on clean and sustainable energy, ocean currents have emerged as a promising source. Traditional hydraulic turbines perform poorly in low-velocity ocean currents, limiting efficient energy extraction. This study introduces a novel multi-grating triboelectric nanogenerator (MG-TENG) that harnesses vortex-induced vibrations for energy harvesting, particularly effective in low-velocity marine environments. Our device not only converts ocean current energy into electricity but also measures flow velocity, addressing two critical needs. Structural improvements to the MG-TENG have boosted its output power by 33.5 times over conventional designs, while durability tests confirm its reliability under sustained operation. A new double-cylinder configuration extends the range of measurable velocities from 0.3 to 0.65 m/s, enhancing the device's versatility. These findings suggest that MG-TENG could serve as both a power supply and a velocity sensor, presenting an innovative solution for energy harvesting in low-velocity ocean currents.

© 2025 Author(s). All article content, except where otherwise noted, is licensed under a Creative Commons Attribution (CC BY) license (<https://creativecommons.org/licenses/by/4.0/>). <https://doi.org/10.1063/5.0250873>

## I. INTRODUCTION

As global energy demands and environmental concerns grow, there is increasing interest in renewable energy sources such as ocean, wind, and solar power.<sup>1</sup> Ocean energy, unlike other sources, is stable and less dependent on seasonal or weather variations,<sup>2,3</sup> making it ideal for powering marine observation equipment, ocean platforms, and other marine devices.<sup>4–6</sup> Ocean current energy, a key component of ocean energy, offers high stability and density, with a global potential exceeding  $5 \times 10^6$  MW.<sup>7</sup> However, traditional ocean current generators, primarily hydraulic turbines, are inefficient in low-velocity conditions and incur high maintenance costs.<sup>8,9</sup> These systems rely on mechanical energy transfer through gearboxes, requiring higher startup velocities that limit their ability to harness energy in slower currents.<sup>10,11</sup> The inefficiency of conventional methods has hindered the broader adoption of marine renewable energy, highlighting an urgent need for efficient solutions that can capture energy at low velocities.<sup>12–14</sup>

Vortex-induced vibration (VIV) devices have recently emerged as a promising, cost-effective solution for low-velocity ocean current energy generation.<sup>15</sup> These devices leverage ocean currents to create vibrations that can be converted into power, offering significant potential for various applications.<sup>16,17</sup> VIV devices are generally classified into piezoelectric and electromagnetic systems.<sup>18</sup> While piezoelectric devices use materials that generate voltage through deformation, their effectiveness depends on advances in material technology.<sup>19</sup> Alternatively, VIV devices with electromagnetic generators, like the VIVACE (Vortex-Induced Vibration for Aquatic Clean Energy) series, deliver a higher power output but require a larger equipment and present maintenance challenges.<sup>20,21</sup> Their adaptability to underwater environments also remains an area of ongoing research and development.

Triboelectric nanogenerators (TENGs) offer a compelling alternative for marine energy harvesting, particularly in low-frequency, low-velocity ocean conditions.<sup>22</sup> TENGs, owing to their suitability for



low-frequency energy sources, have been widely studied and applied across fields, including measurement systems,<sup>23,24</sup> renewable energy,<sup>25,26</sup> environmental monitoring,<sup>27,28</sup> and wearable devices.<sup>29,30</sup> Additionally, their structural flexibility may support various marine applications, such as powering microsensors deployed in ocean environments.<sup>31</sup> Among different TENG configurations, the multi-grating design has shown superior performance compared to other modes, with further optimizations yielding enhanced power output.<sup>32</sup> These features make TENGs highly effective as self-powered sensors, broadening their utility in environmental monitoring and other sensing applications.<sup>30,33</sup>

Building on this background, this study presents a novel nanogenerator for harnessing ocean current energy by utilizing a vortex-induced vibration (VIV) device as a triboelectric ocean current velocity sensor (TCVS). The proposed TCVS generates electrical signals correlated with ocean current frequency, allowing it to both measure current velocity and supply power to various low-power seabed sensors. This dual capability makes the TCVS uniquely advantageous over traditional flow meters, which lack power generation, and turbines, which cannot measure flow speed. The TCVS has potential applications in powering conductivity, temperature, and depth (CTD) sensors to support marine research, operating seabed radiation sensors for real-time monitoring, enabling undersea communications, and wirelessly charging small autonomous underwater vehicles (AUVs), as illustrated in Fig. 1. While currently most suited for localized energy supply, future adaptations could expand its applicability across diverse marine environments.

Specifically, to enhance the power output, we integrate the VIV based ocean energy harvester with a multi-grating triboelectric nanogenerator (MG-TENG). Through experimental validation, a strong relationship was confirmed between the vibration frequency of a cylindrical oscillator in VIV and ocean current velocity. The harvester's double-cylinder, multi-grating design overcomes typical lock-in interval spacing issues associated with VIV, and structural optimizations improved the MG-TENG's output power by approximately 30 times compared to conventional models. This hybrid system demonstrates substantial potential as a self-powered ocean current velocity sensor and subsea

micropower source, providing a versatile solution for sustainable energy harvesting and flow monitoring in marine settings. This paper is organized as follows: Sec. II describes the experimental methods employed and Sec. III presents and analyzes measured results. Finally, key findings and future research directions are summarized in Sec. IV.

## II. EXPERIMENTAL DESIGN AND METHODOLOGY

This section provides an overview of the experimental framework, including the operational principles, structural design, and methodology of the proposed TCVS, which integrates a VIV device with an MG-TENG for water current velocity measurement and energy harvesting. First, the section introduces the overall experimental setup and framework. It then elaborates on the operational principles of VIV and MG-TENG, focusing on the mechanism of electron transfer in TENGs. Subsequently, the numerical methods employed to validate the proposed design are described in detail. Finally, the section concludes with the results of durability testing for the designed nanogenerator, highlighting its reliability and performance over extended operation cycles.

### A. Overall experimental setup

The experimental setup, illustrated in Fig. 2(a), integrates the TCVS device, a circulating flume, an oscilloscope for voltage measurement, a flow meter, a displacement meter, and a data-processing computer. The TCVS device is shown in Fig. 2(b), with its VIV and MG-TENG components depicted in Fig. 2(c). The cylindrical oscillator generates vibrations whose frequency corresponds to the water current velocity. A dual-cylinder oscillator design, with different lock-in intervals, addresses challenges associated with VIV lock-in intervals, ensuring a clear correlation between vibration signals and water velocity. The structural design of the water energy harvesting component, as shown in Fig. 2(d), enables continuous vibration in the water current, producing a reliable motion signal. Figure 2(e) displays the physical setup of the circulating flume, completing the experimental configuration.

The complete experimental framework is depicted in Fig. 3. The TCVS generates electric signals through the MG-TENG, which are

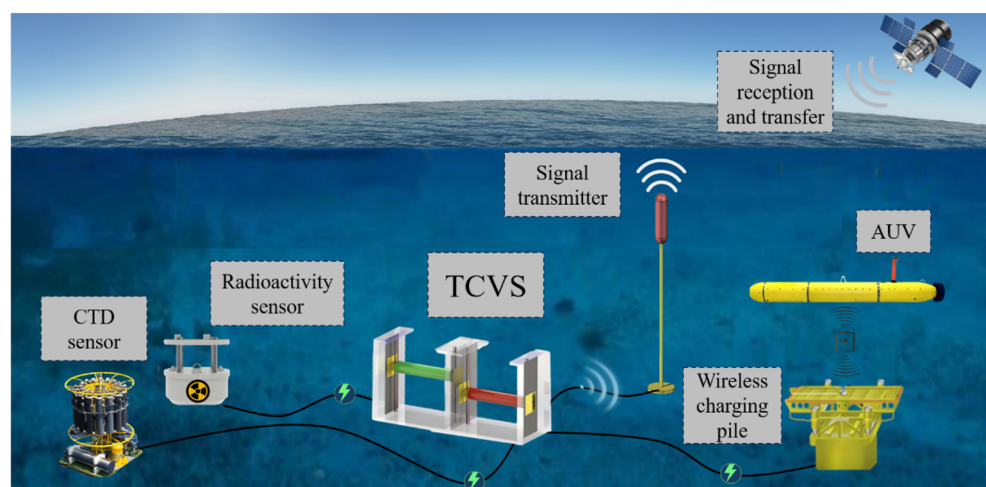
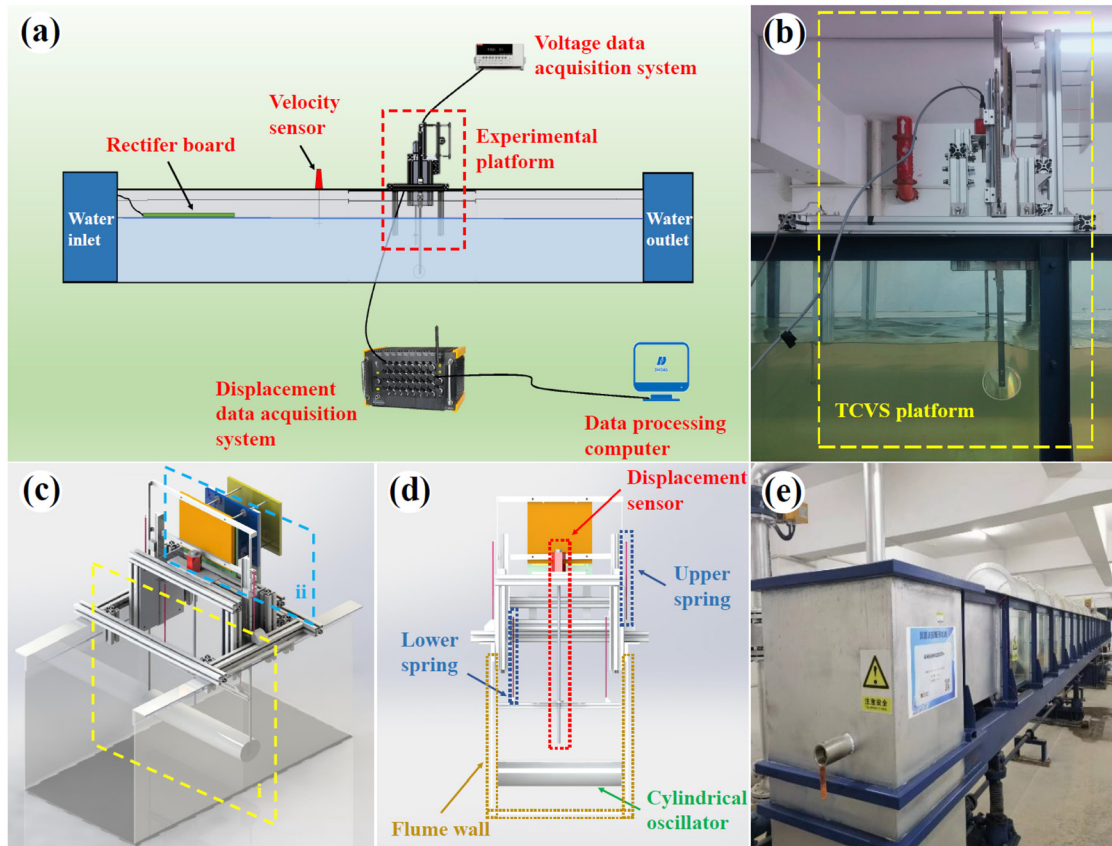


FIG. 1. Schematic of the proposed triboelectric ocean current velocity sensor and its subsea applications.





**FIG. 2.** Schematic and physical diagrams of the experimental platform and components. (a) Schematic diagram of the experimental setup. (b) Physical representation of the TCVS. (c) Model diagram of the TCVS, highlighting the VIV and the TENG components. (d) Identification of the VIV device components and their labels. (e) Physical illustration of the circulating flume.

transmitted to a signal acquisition device. These signals are analyzed using the fast Fourier transform (FFT) technique to extract their dominant frequency  $f_d$ . The extracted frequency is compared against a reference, and a polynomial fitting process is applied to determine the corresponding water current velocity. This approach enables accurate velocity measurements, particularly in low-velocity conditions.

### B. Operational principle of VIV

Vortex-induced vibrations (VIV) occur when a fluid flows past a bluff body, generating a repeating pattern of vortices in its wake.<sup>34</sup> This oscillation can induce significant structural vibrations, potentially leading to fatigue and catastrophic failure in engineering systems like offshore platforms, marine risers, and pipelines.<sup>35</sup> Managing VIV is

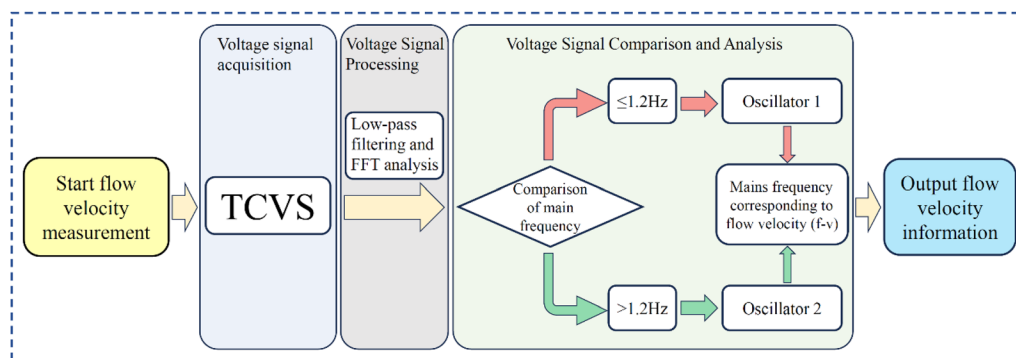


**FIG. 3.** An overview of the designed triboelectric ocean current velocity sensor (TCVS).



essential to maintaining the structural integrity of these systems, especially in “lock-in” regions where the frequency of vortex shedding matches the structure’s natural frequency, resulting in large-amplitude vibrations.<sup>36</sup> Recently, attention has shifted from simply mitigating VIV to harnessing the energy it generates. This has led to applications in renewable energy, where devices convert mechanical energy from VIV into electricity. Systems like the VIVACE converter, which captures energy from marine currents, have demonstrated the potential of this approach.<sup>20</sup> The mechanism of VIV is illustrated schematically in Fig. 4. A cylindrical structure, elastically mounted in a current flume, oscillates transversely under the influence of vortex shedding from a uniform water flow.

This transverse motion, constrained to a single degree of freedom, is governed by the classical mass-spring-damper model,

$$m\ddot{y} + c\dot{y} + ky = F_y, \quad (1)$$

where  $m$  represents the structural mass,  $k$  is the stiffness,  $y$ ,  $\dot{y}$ , and  $\ddot{y}$  denote the position, velocity, and acceleration, respectively,  $F_y$  is the fluid-induced force, and  $c$  is the equivalent linear damping. The natural frequency in water is determined using

$$f_n = \frac{1}{2\pi} \sqrt{\frac{k}{m + m_a}}, \quad U^* = \frac{U}{f_n D}, \quad (2)$$

where  $m_a$  is the added mass due to fluid and  $U^*$  is the reduced velocity defined using the flow velocity of  $U$  and the cylinder diameter of  $D$ . The total mechanical power  $P_m$  extracted by the oscillator is

$$P_m = \frac{1}{T} \int_0^T F_y \dot{y} dt = \frac{1}{T} \int_0^T (m\ddot{y} + c\dot{y} + ky) \dot{y} dt, \quad (3)$$

where  $T$  is the device’s oscillation period.

### C. Operational principle of MG-TENG

The TENG operates based on the principle of electron transfer between materials with differing electron-donating and electron-accepting tendencies. When these materials come into contact, electrons transfer from one material to the other. Upon separation due to an external force, this process creates positive and negative surface charges and generates an electric potential difference. The resulting electric field drives electron flow through an external circuit. The

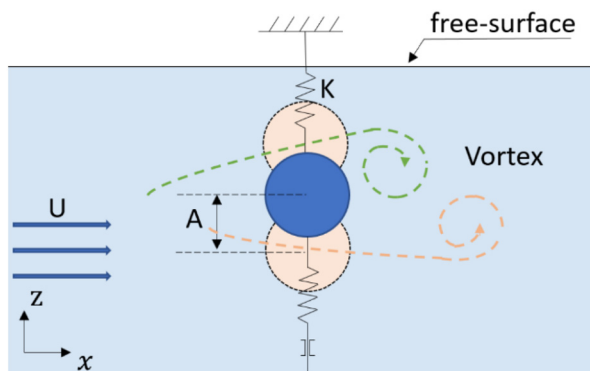


FIG. 4. Schematic diagram illustrating the operational principle of a VIV device.

freestanding triboelectric layer in the device can be classified as either dielectric or metallic, depending on the chosen materials. A schematic diagram illustrating the operational principles of two different SF-TENG (sliding-mode freestanding TENG) models is given in Fig. 5.

In both designs, the distance between electrode A and electrode B is denoted as  $g$ . A freestanding dielectric layer, with the same dimensions as electrodes A and B, is positioned on the metallic electrode. The distance between the bottom surface of the freestanding dielectric layer and the metal is labeled  $h$ , and the width of the structure is  $w$ . For the dielectric-type SF-TENG shown in Fig. 5(a), the freestanding dielectric layer is composed solely of dielectric material. In contrast, the metal-type SF-TENG depicted in Fig. 5(b) incorporates a metal film deposited on the backside of the freestanding dielectric layer. Assuming a small segment  $dk$  of the dielectric layer’s bottom surface contains a frictional charge with a surface charge density of  $-\sigma$ , the total charge on electrodes A and B can be expressed as  $-\sigma wdk$  in a short-circuit scenario. From this, the total charge on electrodes A and B, the charge transfer through the load, and the short-circuit current can be determined through theoretical calculations. Among these, the energy generation efficiency differs significantly. Previous studies<sup>37</sup> have demonstrated that the TENG model in Fig. 5(b) exhibits a larger rise and fall of capacitance and a more rapid rise in open-circuit voltage during a moving stroke compared to the TENG model in Fig. 5(a). However, the capacitance and voltage at the end of the stroke are the same for both models. Notably, the amount of transferred charge at the end of the stroke is also identical. The primary distinction in the output performance lies in the variation of the open-circuit voltage curve. Although limited literature has comparatively analyzed all three TENG models shown in Figs. 5(a)–5(c), the TENG configuration depicted in Fig. 5(c) has gained prominence in recent years as an improved model of the first two.<sup>38,39</sup> There are two main considerations for this preference: (1) The gap between electrodes A and B in Figs. 5(a) and 5(b) increases the wear potential of the dielectric layer, reducing durability. (2) The TENG model in Fig. 5(c) involves two dielectrics in contact with each other. This configuration can achieve a larger potential difference between the two dielectrics compared to the potential difference between the electrodes and dielectrics in Figs. 5(a) and 5(b). Consequently, the TENG model in Fig. 5(c) can produce a higher open-circuit voltage, making it a more efficient and durable option.

A two-grating sliding freestanding dielectric layer TENG is used to demonstrate the operational principle of multi-grating configurations, as shown in Fig. 5(c). The electrodes, each of length  $L$  along the sliding direction, are spaced  $g$  apart. The generator produces AC voltage and current by driving the upper slider back and forth. In this setup, the slider is made of polyamide (PA) and the electrodes are made of copper. The electrode surfaces are coated in fluorinated ethylene propylene (FEP). When FEP and PA come into contact and undergo relative motion, FEP, being more electronegative, gains electrons via charge transfer. This induces equal but opposite charges on the FEP and PA surfaces, explained as follows:

- (i) when the PA slider completely overlaps the left electrode, negative charges accumulate on the upper surface of the left electrode;
- (ii) as the slider moves rightward, positive charges flow through the circuit from the right electrode to the left electrode;



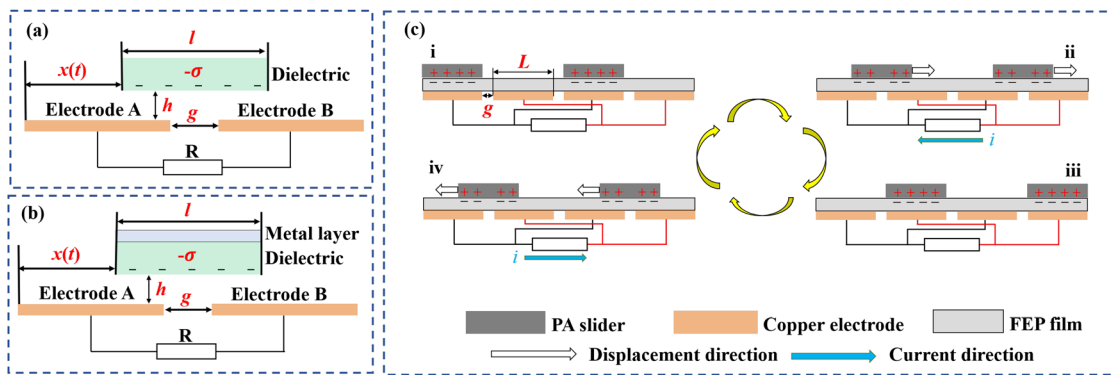


**FIG. 5.** Schematic of two different SF-TENG (sliding-mode freestanding TENG) models: (a) dielectric SF-TENG model; (b) metal SF-TENG model; and (c) a single work cycle of a 2-grating TENG.

- (iii) when the slider aligns fully with the right electrode, all positive charges have transferred to the left electrode. This completes the first half of the cycle;
- (iv) the slider then returns to the left electrode, reversing the motion direction and generating a reverse current in the circuit. This completes the second half of the cycle.

To verify the correlation between the voltage frequency and the motion frequency of the designed MG-TENG, numerical simulations were performed using COMSOL Multiphysics. A 16-grating MG-TENG configuration was selected to optimize output under low-amplitude, low-frequency VIV conditions. For example, the results illustrated in Fig. 6 include three prescribed displacement profiles. Our simulations confirm that the output voltage frequency is directly proportional to the oscillatory motion frequency of the slider. A strong correlation between the input motion and the output voltage signal is established, demonstrating the feasibility of using the TENG's output voltage frequency to determine the sliding displacement frequency.

## D. Design and testing of the nanogenerator

### 1. Structural design

The conventional freestanding triboelectric-layer mode MG-TENG slider comprises a single layer of either metallic or nonmetallic material, referred to as type A in Fig. 7(a). During the sliding process, negative charges on the surface of PA fabric are adsorbed by a FEP film, resulting in positive charges on the PA fabric. Given that the PA fabric's area is half that of the FEP film, the positive charge density on the PA surface is twice that of the negative charge density on the FEP surface, assuming uniform charge distribution as shown in Fig. 7(b-I). In the process of reciprocating movement of the slider, the superposition of positive and negative charges generates alternating electric fields at the copper electrodes, leading to alternating potential differences between adjacent electrodes.

### 2. Performance optimization

Figure 8(a) shows the voltage curve of type A under specific test conditions: a reciprocating motion period of  $T = 1.1$  s, a motion amplitude of  $\zeta = 16$  cm, a  $m = 200$  g weight applied as positive pressure, and a FEP film size of  $16 \times 16$  cm. The peak-to-peak voltage

(VP-P) under these conditions is 451 V. To enhance the output, an aluminum (Al) conductor layer ( $45 \mu\text{m}$  thick) was added to the back of the PA fabric (type B in Fig. 7). When the Al conductor and PA fabric are combined in contact, the electrons are transferred from the surface of PA fabric to the surface of Al conductor because the Al conductor is more accessible to electrons than PA fabric, as demonstrated in Fig. 7(c-I).<sup>40,41</sup> When the PA fabric slides on the FEP film, as in Fig. 7(b-II), we zoom in and analyze one of the sliders, as in Fig. 7(c-II). The FEP film acquires electrons from surface of PA fabric, and thus, the surface of PA fabric is positively charged, at which point the upper and lower surfaces of Al conductor generate induced charges in the electric field of the charge on the FEP film. The copper electrode under the FEP film obtains a higher potential in this case compared to the case where no Al conductor is involved. Testing type B under the same conditions as type A yielded a significant improvement in VP-P to 1113 V, with enhanced output uniformity as plotted in Fig. 8(b).

When a portion of the PA fabric slides out of the FEP film [Fig. 7(b-II)], the potential on the upper surface of Al conductor increases due to the lack of negative charge on the FEP film. At this point connecting all Al conductors with a wire (type C in Fig. 7), the Al conductor with increased potential will transport positive charge to the others [Figs. 7(b-III) and 7(c-III)]. The other Al conductors thus also increase their potential due to the increase in charge, which is further increased at the copper electrode. Under identical test conditions, type C achieved an impressive VP-P of 1599 V with minimal fluctuations in the peak output as plotted in Fig. 8(c). A comparison of the total output work reveals that the type B structure's output was 10.7 times that of type A, while type C delivered 33.5 times the output work of type A. These results validate the structural optimizations as highly effective in improving the MG-TENG's performance.

### 3. Durability testing

Durability tests were conducted on a 4-grating MG-TENG to evaluate sustained performance. The test platform, depicted in Fig. 9, consists of a servo motor driving the electrode plate in a reciprocating motion. The setup includes a fixed grating plate, adjustable counterweights, and connections to various resistive loads. Voltage data were recorded using an oscilloscope. The test, performed at a frequency of 1 Hz with a 200 g load, demonstrated that after 30 000 cycles, the MG-



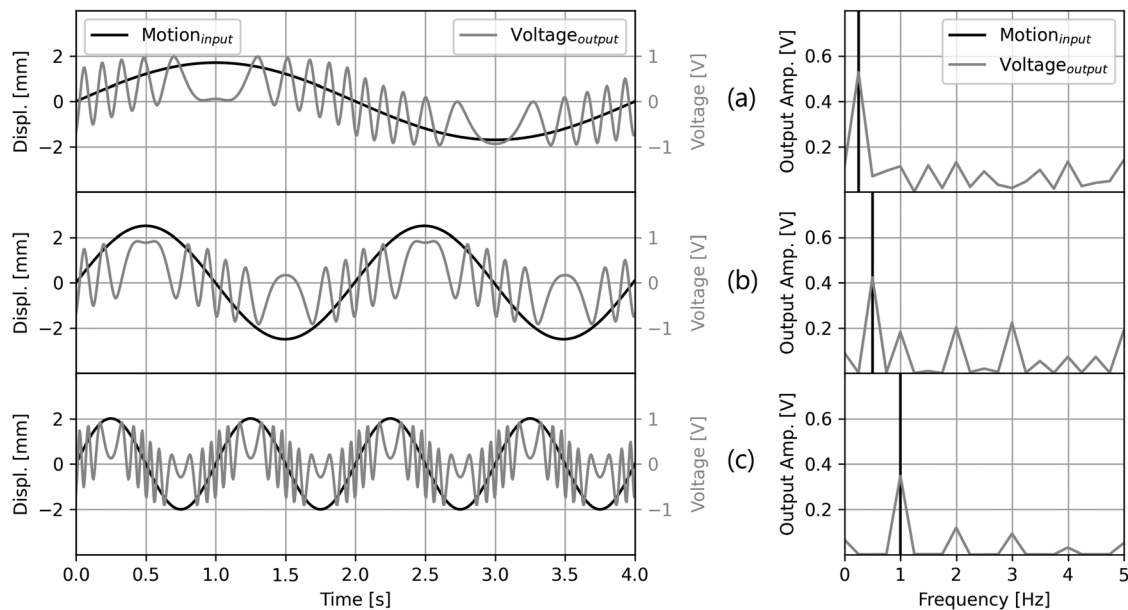


**FIG. 6.** Correlation between input motion displacement and output voltage for three different conditions: (a) input motion at 0.25 Hz; (b) input motion at 0.5 Hz; and (c) input motion at 1.0 Hz.

TENG maintained over 90% of its initial voltage output, indicating excellent durability as shown in Fig. 10.

### III. RESULTS AND DISCUSSION

#### A. Double-cylinder experiments and vibration analysis

The effect of double-cylinder implementation was evaluated by varying spring stiffness and adding counterweights. These experiments analyzed the relationship between vibration frequency and water current velocity under different flow conditions. To minimize the damping effect of conventional displacement sensors, a magnetostrictive displacement sensor was employed to measure absolute displacement. Displacement signals were acquired and processed over durations of 60–90 s, selecting stable 30 s waveforms for analysis. The experimental

oscillator weighed 2755 g, and water current velocities ranged from 0.3 to 0.65 m/s. For example, Fig. 11 illustrates the vibration process with a period of 0.88 s (i.e., 1.14 Hz in frequency). Accordingly, displacement signals were recorded for spring stiffness values of 150 and 200 N/m for various conditions, as plotted in Fig. 12.

As illustrated in Fig. 13(a), a fast Fourier transform (FFT) analysis of these signals reveals that vibration frequency increased with water current velocity. Resonance occurred when the vortex shedding frequency matched the cylinder's natural frequency. The lock-in interval, where vibration frequency equaled vortex shedding frequency, spanned 0.45–0.5 m/s for 200 N/m and 0.5–0.55 m/s for 150 N/m. The combined results given in Fig. 13(b) allow derivation of the water current frequency relationship, which demonstrates linearity between

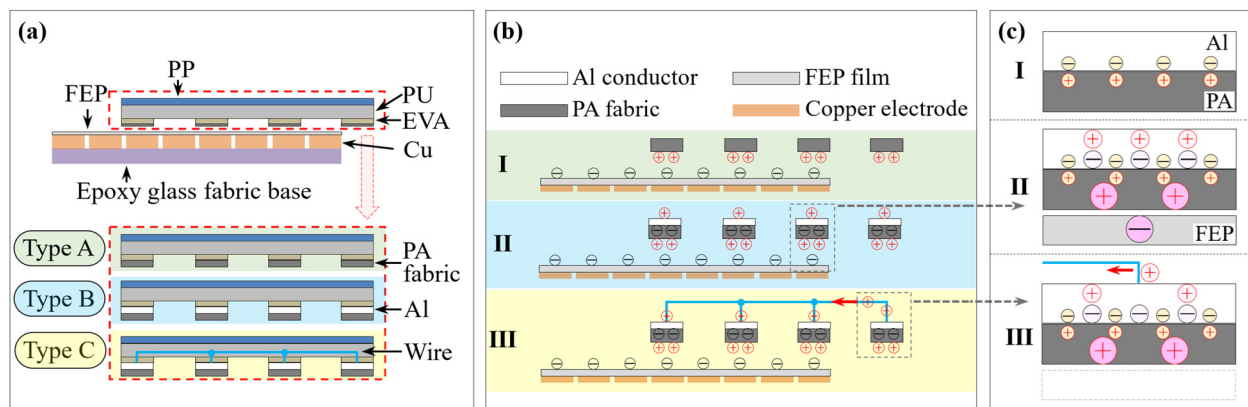


**FIG. 7.** Schematic diagrams illustrating the structure and charge transfer mechanisms of the MG-TENG during operation. (a) The schematic of a 4-grating TENG with three distinct slider structures. (b) The charge distribution and transfer processes for the three slider types. (c) Schematic diagram of charge changes inside conductor and dielectric.



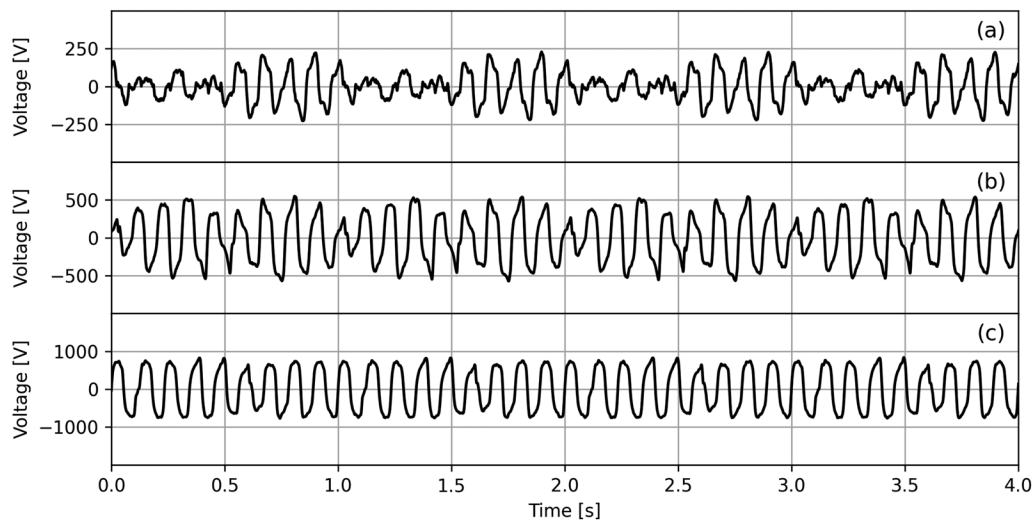


**FIG. 8.** Voltage curves for three slider types during sliding tests. (a) The results for the conventional structure featuring only PA fabric. (b) The results after incorporating an AI conductor. (c) The results with the addition of both an AI conductor and connecting wire.

water current velocity and vibration frequency. This ensures distinguishable vibration frequencies in the low-velocity range (below 0.65 m/s). Measured vibration frequencies ranged from 0.867 to 1.400 Hz, as shown in Fig. 13(c).

### B. MG-TENG performance

As shown in Fig. 14(a), the MG-TENG part primarily consists of three components. The first component is the grating fixed plate, which is rigidly connected to the cylindrical oscillator. The vertical section of this part includes 16 grating plates that contact with the other components. The second component is the electrode fixed plate, which is connected to a slide bar and a fixed pulley fixed plate. These three plates are combined as one unit, as shown in Fig. 14(b). The electrode fixing plate features four through holes that allow it to be positioned on the left side. The side facing the grating fixing plate is used for placing the electrodes and inducing the frictional electric signal. The electrode fixing plate and the fixed pulley fixing plate are positioned in the middle. By adjusting the weights mounted on the pulleys, the pressure

between the plates can be controlled to ensure that the TENG has a high-power generation efficiency. The combination fixing plate is placed on the right side. The mechanical structure is kept balanced, and facilitating pressure between the plates is satisfied for adjustment. To ensure the recognizability of the electrical output, the power generation capacity of TCVS under low water current velocity is tested. The theoretical model encompasses the voltage source model and the electric current source model, which are sketched in Fig. 14(c). TCVS can light up the ZJOU character made up of LED beads, as depicted in Fig. 14(d). In the test, electric currents with load resistances of 10 k  $\Omega$  to 1 G  $\Omega$  are tested by using 16-grating-TENG and weight of 200 g as positive pressure, and the results are shown in Fig. 15(a).

It can be observed that the TCVS exhibits a pattern where the power initially reaches its peak and then decreases back to stabilize under four different water current velocities. This behavior can be attributed to the varying power models of MG-TENG. When the value of the external circuit resistance is less than the internal resistance, the MG-TENG exhibits a voltage source characteristic. The electric current decreases as the value of the external circuit resistance increases, as

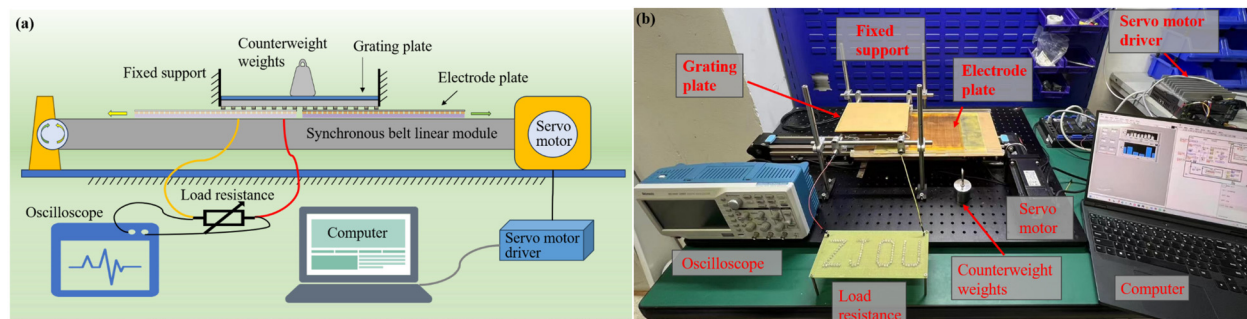


**FIG. 9.** Schematic and physical representation of the sliding test setup. (a) Schematic diagram illustrating the sliding test mechanism. (b) Physical photograph of the sliding test apparatus.



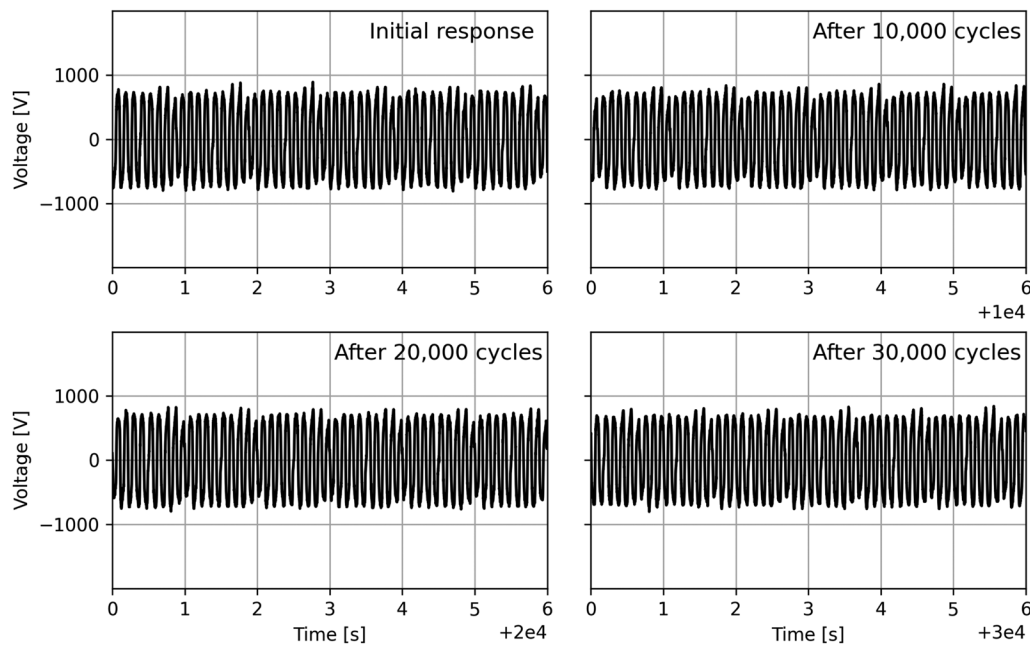


FIG. 10. Durability test results, showing the time series of voltage output after 30 000 cycles.

shown in Fig. 15(b). When the external circuit resistance is equal to the internal resistance of the MG-TENG, the output power reaches its maximum. Moreover, when the value of the external circuit resistance is much larger than the internal resistance, the MG-TENG exhibits an electric current source characteristic. The electric current remains small and does not change as the external circuit resistance increases. Finally, the output power increases with the increase in the external circuit resistance. The relationship between power output and resistance further confirmed that peak power was achieved under matched resistance conditions.

### C. Power output analysis and capacitor test

The average output power of the 16-grating MG-TENG under varying loads was further analyzed for different positive pressures when the water current velocity ranged from 0.3 to 0.6 m/s, as shown

in Fig. 16. The results indicate that the maximum average power at each pressure occurs within a load range of 500 k  $\Omega$  to 1 M  $\Omega$  under all four water current velocities. After reaching this peak, the average output power decreases and eventually stabilizes. This observation confirms earlier analyses, that is the output power reaches its maximum when the load resistance matches the internal resistance of the MG-TENG. Furthermore, the output power increases as the applied positive pressure grows.

To assess the power supply capability of the TCVS in ocean current energy harvesting, a low-power thermohydrometer was connected to the circuit for testing. Since the TCVS generates an alternating voltage, its output exhibits significant fluctuations, even after rectification via a bridge circuit. To address this, a 4700  $\mu$ F capacitor was added to the circuit to store the TCVS output. Testing conditions included an 8-grating configuration, a flow velocity of 0.5 m/s, and a positive pressure of 400 g. During the experiment, the capacitor charged to 1.495 V

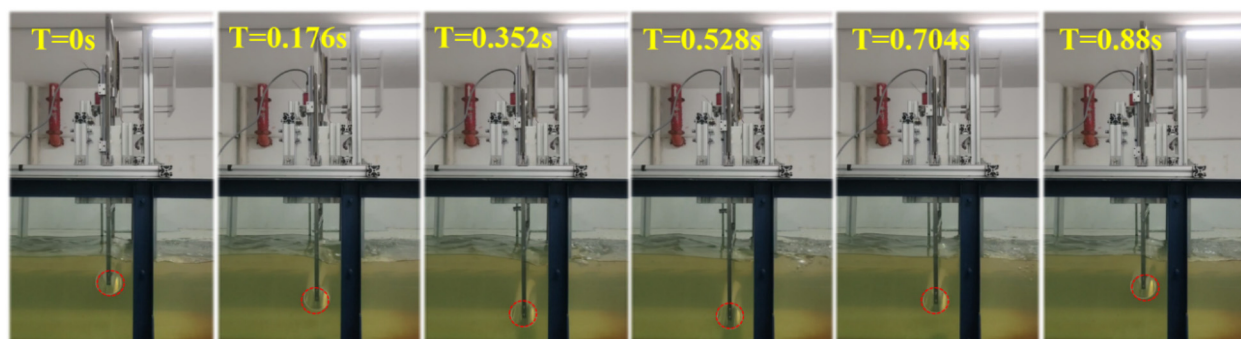
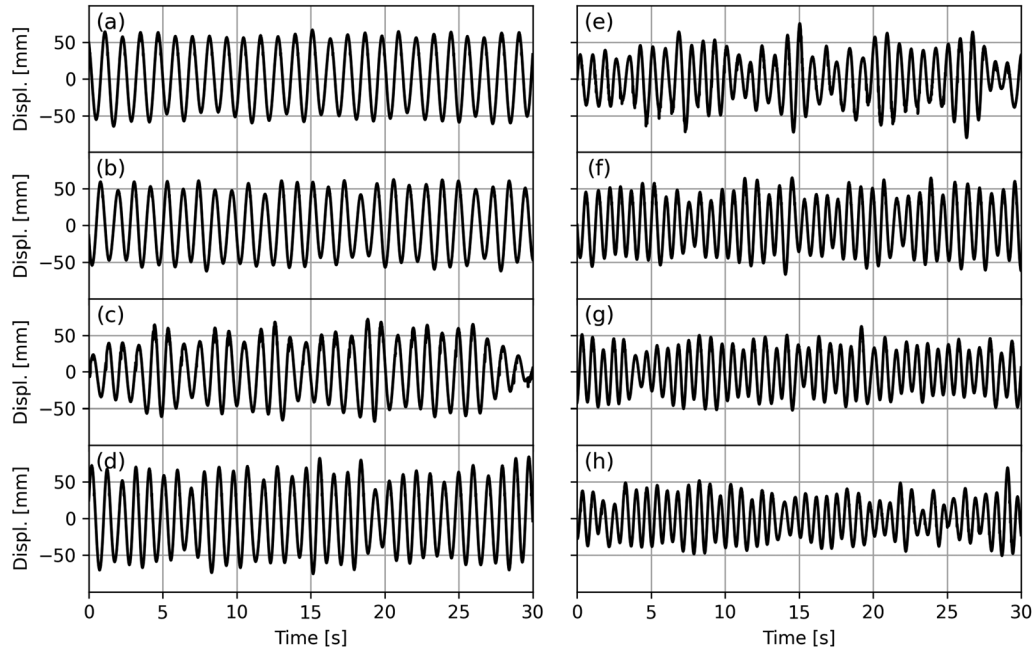
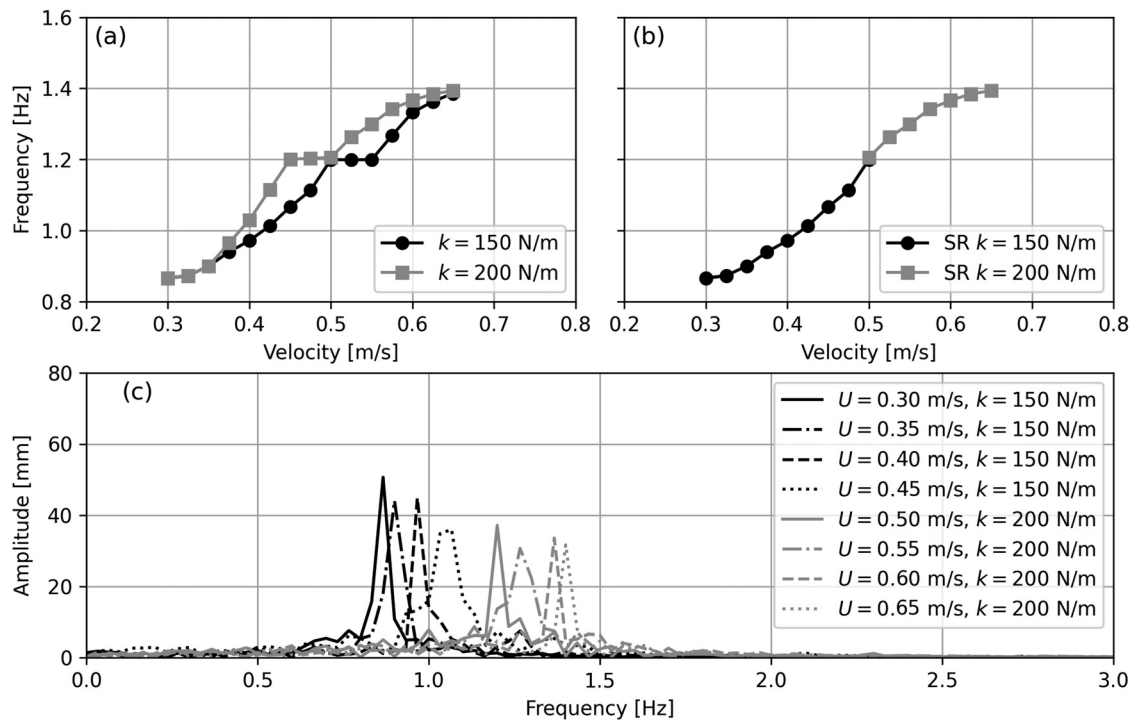


FIG. 11. Vibration process of TCVS with a oscillation period of  $T = 0.88$  s.





**FIG. 12.** Displacement signals of the cylindrical oscillator under two different spring stiffness: (a)  $U = 0.30$  m/s and  $k = 150$  N/m; (b)  $U = 0.35$  m/s and  $k = 150$  N/m; (c)  $U = 0.40$  m/s and  $k = 150$  N/m; (d)  $U = 0.45$  m/s and  $k = 150$  N/m; (e)  $U = 0.50$  m/s and  $k = 200$  N/m; (f)  $U = 0.55$  m/s and  $k = 200$  N/m; (g)  $U = 0.60$  m/s and  $k = 200$  N/m; and (h)  $U = 0.65$  m/s and  $k = 200$  N/m.



**FIG. 13.** Experimental results demonstrating the correlation between water current velocity and device vibration. (a) Main frequency plots of water current velocity for  $k = 150$  and  $200$  N/m. (b) Selected region (SR) highlighted in the main frequency–water current velocity diagram. (c) Principal frequency diagram showing correlations between water current velocities of  $0.3$ – $0.45$  m/s for  $k = 150$  N/m and  $0.5$ – $0.65$  m/s for  $k = 200$  N/m.



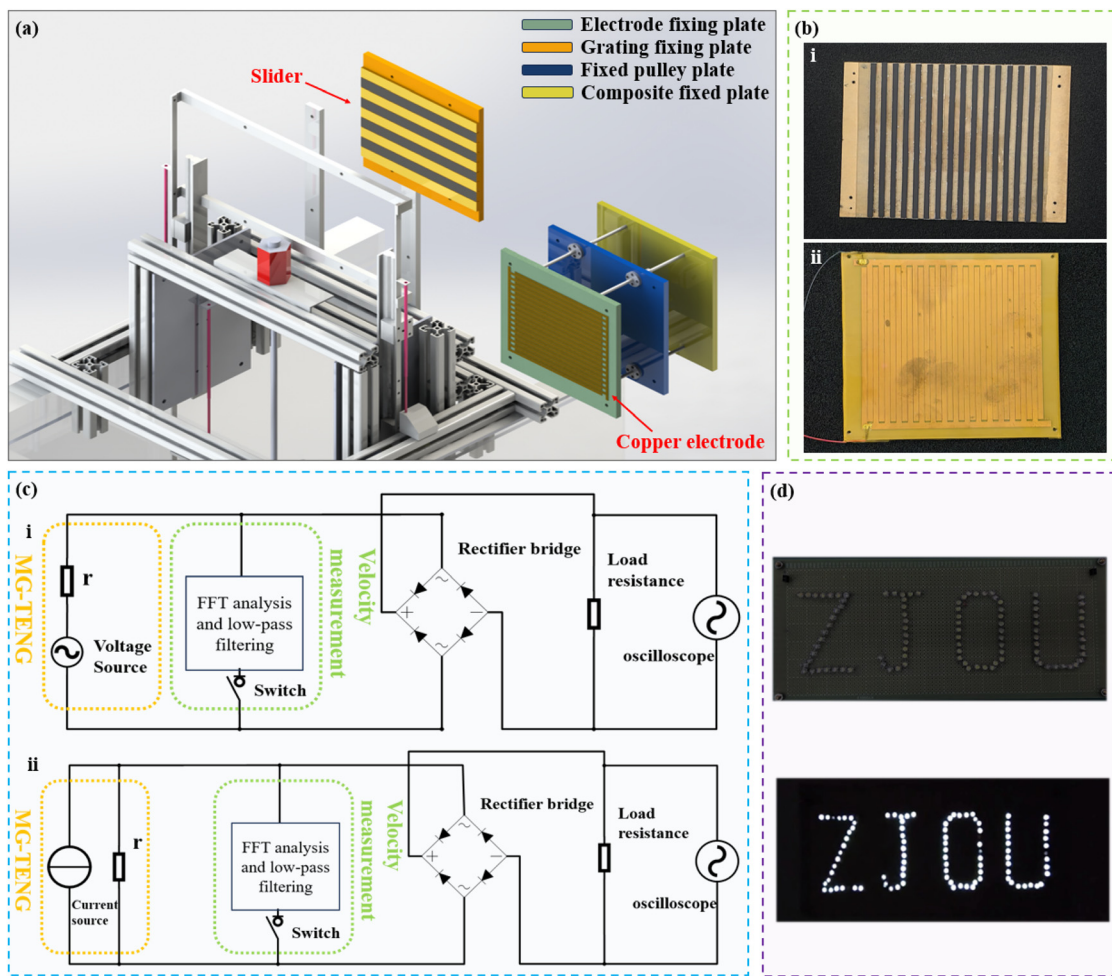


**FIG. 14.** Performance of the designed MG-TENG. (a) Schematic diagram of MG-TENG section. (b) The sliding copper part and the sensing electrode. (c) Schematic diagram of TCVS voltage and current source models for power generation test. (d) Comparison of LED light beads before and after connecting to the circuit.

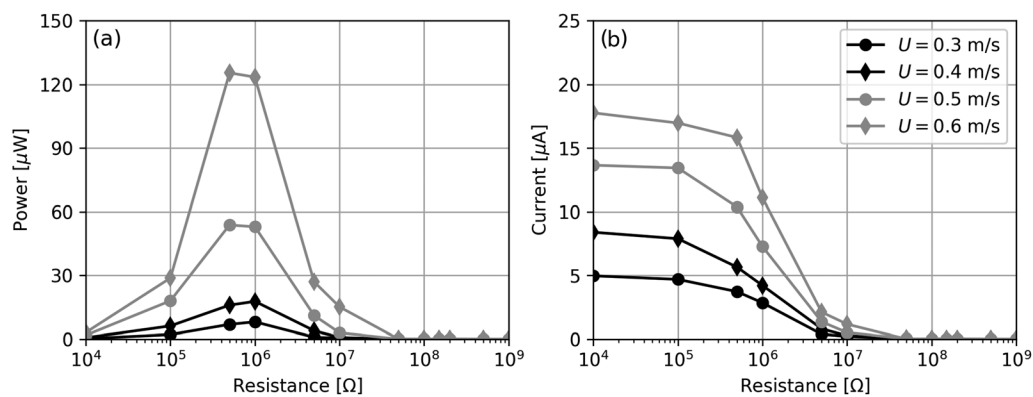


**FIG. 15.** Output capacity of the MG-TENG. (a) Power generation across varying resistance values. (b) Electric current output corresponding to different resistance values.



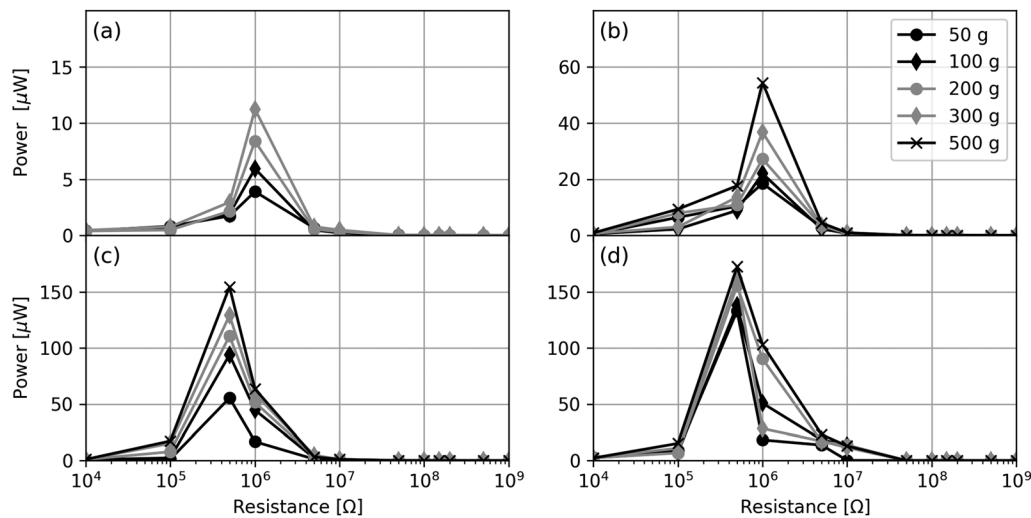


FIG. 16. Average output power for different loads in the circulating flume experiment: (a)  $U = 0.3$  m/s; (b)  $U = 0.4$  m/s; (c)  $U = 0.5$  m/s; and (d)  $U = 0.6$  m/s.

before the thermohydrometer was connected to the circuit. A digital multimeter was used to monitor the capacitor's charging and discharging process, and the voltage–time curve is shown in Fig. 17. The data reveal that the capacitor voltage rose from 0 to 1.495 V over 129 s of charging. Once the thermohydrometer was connected, it operated for approximately 62 s until the voltage dropped to 1.062 V. It was observed that the capacitor recharged to 1.062 V within 47 s. This implies that if the capacitor continues charging for an additional 47 s after reaching 1.062 V, the thermohydrometer can operate for 62 s. By repeating this charging and discharging cycle continuously, the thermohydrometer could maintain perpetual operation.

#### D. Voltage measurement and software interface

Voltage signals were experimentally measured for water current velocities ranging from 0.3 to 0.6 m/s, in intervals of 0.1 m/s, as shown in Figs. 18(a)–18(d). The analysis of the voltage's main frequency, illustrated in Fig. 18(e), reveals that it closely corresponds to the main frequency of the displacement signal. To streamline the measurement process, a custom software application developed using LabVIEW was

employed. This software automatically calculates water current velocity from the voltage data.

A snapshot of the TCVS water current velocity measurement software interface is displayed in Fig. 19(a). On the left side of the interface, voltage signals induced by two sets of oscillators with differing spring stiffness values are shown for a water current velocity of 0.37 m/s. The right side of the interface presents the calculated main frequency of the voltage signals alongside the derived water current velocity value. The TCVS device was further evaluated for its performance in measuring water current velocities under five flow conditions (0.3, 0.4, 0.5, 0.6, and 0.65 m/s). Each condition was measured five times, and the results, including error bars, are presented in Fig. 19(b). Error analysis indicates that the maximum percentage error for these measurements is  $\pm 5\%$ .

These findings confirm the versatility of the TCVS device. It can function not only as a self-powered water current velocity sensor but also as a low-power energy source. The TCVS has the potential to provide energy for various small-scale sensor devices, such as conductivity-temperature-depth (CTD) instruments, seafloor sediment sensors, underwater mooring platforms, and underwater batteries, broadening its applicability in marine environments.

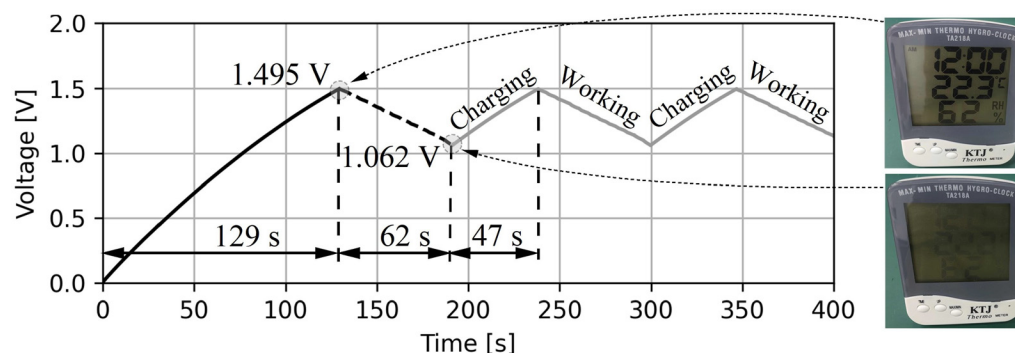
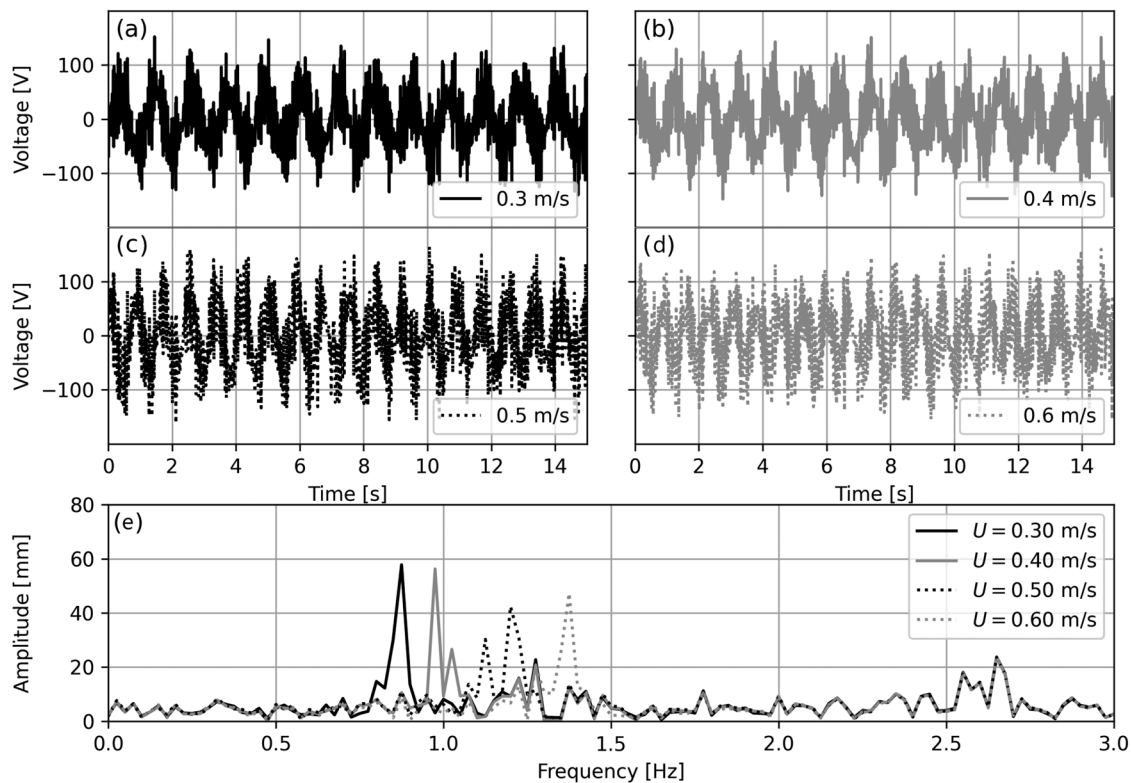


FIG. 17. Capacitor voltage–time curve during TCVS charging of the 4700  $\mu$ F capacitor and powering the thermohydrometer.





**FIG. 18.** Voltage signal of TCVS over various conditions: (a)  $U = 0.3$  m/s; (b)  $U = 0.4$  m/s; (c)  $U = 0.5$  m/s; and (d)  $U = 0.6$  m/s. (e) Main frequency of voltage for water current velocities between 0.3 and 0.6 m/s.

#### IV. CONCLUDING REMARKS

In summary, a triboelectric ocean current velocity sensor (TCVS) device based on MG-TENG and VIV device has been proposed in this study. The experimental results show that TCVS device not only functions as a self-powered ocean current velocity sensor, but also has the

potential to be able to supply power to various other electronic components. The main conclusions are summarized as follows:

- Utilizing the reciprocating motion of the cylinder oscillator to drive the MG-TENG to produce a voltage signal of a specific

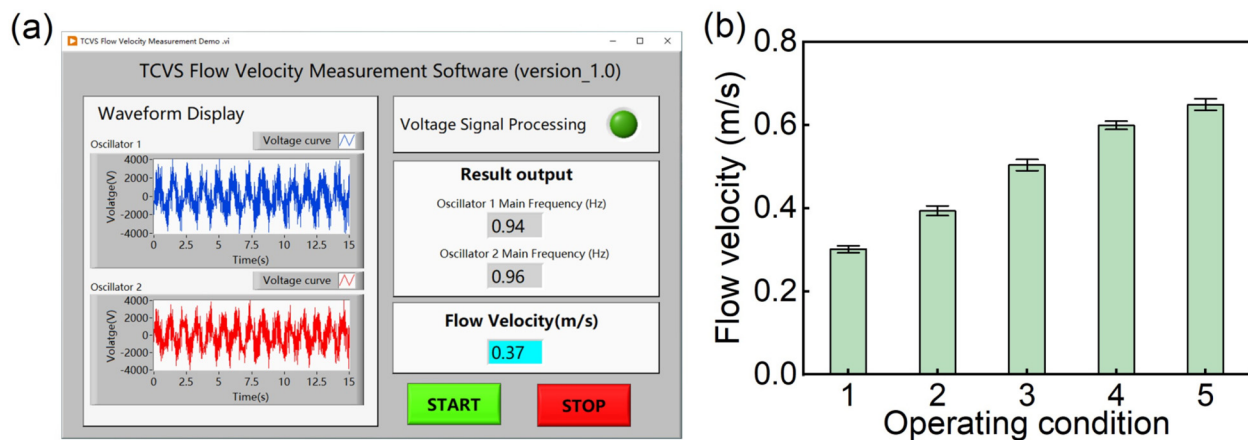


**FIG. 19.** User interface of velocity measurement software and error analysis. (a) Snapshot of TCVS water current velocity measurement software operating at  $U = 0.37$  m/s. (b) Measured flow velocity and corresponding error bar graph for five flow conditions using the TCVS.



frequency, the TCVS device can be accurately used to measure the water current velocity from 0.3 to 0.65 m/s.

- A new multi-grating structure of MG-TENG was developed for greatly improving the output performance. By using the new structure, the output power of the MG-TENG is increased up to 33.5 times that of the conventional structure under the same movement conditions and materials.
- Through the durability test of 30 000 cycles, the MG-TENG used in this study still possessed a power output performance about 90% of the initial state. This indicates that the MG-TENG used in this study has some degree of durability potential.
- The output power of the TCVS device behaves differently at different water current velocities, different load resistances, and different positive pressures. The highest output power occurs at a specific load resistance, and there is a tendency for the output power to be higher at higher positive pressures and faster water current velocities.

## ACKNOWLEDGMENTS

We thank the University of Duisburg-Essen for supporting this work through its Open Access Publication Fund.

The first author acknowledges the financial support from the National Natural Science Foundation of China (No. 52301342).

## AUTHOR DECLARATIONS

### Conflict of Interest

The authors have no conflicts to disclose.

## Author Contributions

**Peng Xu:** Conceptualization (equal); Data curation (equal); Funding acquisition (equal); Validation (equal); Writing – original draft (lead). **Mingjie Hong:** Data curation (equal); Investigation (equal); Software (equal); Writing – original draft (supporting). **He Li:** Conceptualization (equal); Formal analysis (equal); Software (equal); Validation (equal). **Chenlu Song:** Conceptualization (equal); Formal analysis (equal); Investigation (equal); Project administration (equal). **Ould el Moctar:** Conceptualization (equal); Resources (equal); Supervision (equal); Writing – review & editing (supporting). **Changqing Jiang:** Conceptualization (equal); Formal analysis (equal); Supervision (equal); Writing – review & editing (lead).

## DATA AVAILABILITY

The data that support the findings of this study are available from the corresponding author upon reasonable request.

## REFERENCES

- J. Gong, Y. Li, C. Suo, and J. Lv, "Planning regional energy system with consideration of energy transition and cleaner production under multiple uncertainties: A case study of Hebei Province, China," *J. Cleaner Prod.* **250**, 119463 (2020).
- Y. Yao, T. Jiang, L. Zhang, X. Chen, Z. Gao, and Z. L. Wang, "Charging system optimization of triboelectric nanogenerator for water wave energy harvesting and storage," *ACS Appl. Mater. Interfaces* **8**, 21398–21406 (2016).
- Y. Zhang, Y. Zhao, W. Sun, and J. Li, "Ocean wave energy converters: Technical principle, device realization, and performance evaluation," *Renewable Sustainable Energy Rev.* **141**, 110764 (2021).
- A. Clément, P. McCullen, A. Falcão, A. Fiorentino, F. Gardner, K. Hammarlund, G. Lemonis, T. Lewis, K. Nielsen, S. Petroncini *et al.*, "Wave energy in europe: Current status and perspectives," *Renewable Sustainable Energy Rev.* **6**, 405–431 (2002).
- M. Richter, M. E. Magana, O. Sawodny, and T. K. Brekken, "Nonlinear model predictive control of a point absorber wave energy converter," *IEEE Trans. Sustainable Energy* **4**, 118–126 (2013).
- Z. L. Wang, J. Chen, and L. Lin, "Progress in triboelectric nanogenerators as a new energy technology and self-powered sensors," *Energy Environ. Sci.* **8**, 2250–2282 (2015).
- J. Wang, H. Wang, Y. Liu, L. Chen, and J. Tang, "The development of marine renewable energy in China: Prospects, challenges and recommendations," *IOP Conf. Ser.: Earth Environ. Sci.* **121**, 052079 (2018).
- R. Ahamed, K. McKee, and I. Howard, "Advancements of wave energy converters based on power take off (PTO) systems: A review," *Ocean Eng.* **204**, 107248 (2020).
- J. Chen, J. Yang, Z. Li, X. Fan, Y. Zi, Q. Jing, H. Guo, Z. Wen, K. C. Pradel, S. Niu *et al.*, "Networks of triboelectric nanogenerators for harvesting water wave energy: A potential approach toward blue energy," *ACS Nano* **9**, 3324–3331 (2015).
- M. Kamoji, S. Kedare, and S. Prabhu, "Performance tests on helical Savonius rotors," *Renewable Energy* **34**, 521–529 (2009).
- P. Jaohindy, S. McTavish, F. Garde, and A. Bastide, "An analysis of the transient forces acting on Savonius rotors with different aspect ratios," *Renewable Energy* **55**, 286–295 (2013).
- G. Calcagno, F. Salvatore, L. Greco, A. Moroso, and H. Eriksson, "Experimental and numerical investigation of an innovative technology for marine current exploitation: The Kobold turbine," in *ISOPE International Ocean and Polar Engineering Conference (ISOPE, 2006)*, Paper No. ISOPE-I-06-043.
- J. VanZwieten, F. Driscoll, A. Leonessa, and G. Deane, "Design of a prototype ocean current turbine—Part I: Mathematical modeling and dynamics simulation," *Ocean Eng.* **33**, 1485–1521 (2006).
- P. Qian, B. Feng, H. Wen, X. Jiang, Y. Ying, Y. Si, and D. Zhang, "Maximum power point tracking for triboelectric nanogenerator based wave energy converters," *Nano Energy* **98**, 107249 (2022).
- E. Molino-Minero-Re, M. Carbonell-Ventura, C. Fisac-Fuentes, A. Mànuel-Làzaro, and D. M. Toma, "Piezoelectric energy harvesting from induced vortex in water flow," in *IEEE International Instrumentation and Measurement Technology Conference Proceedings (IEEE, 2012)*, pp. 624–627.
- K. Narendran, K. Murali, and V. Sundar, "Investigations into efficiency of vortex induced vibration hydro-kinetic energy device," *Energy* **109**, 224–235 (2016).
- M. O. Awadallah, C. Jiang, and O. el Moctar, "Numerical study into the impact of fixed upstream cylinder diameter ratios on vibration of leeward tandem cylinders," *Ocean Eng.* **285**, 115367 (2023).
- A. Erturk and D. J. Inman, "An experimentally validated bimorph cantilever model for piezoelectric energy harvesting from base excitations," *Smart Mater. Struct.* **18**, 025009 (2009).
- R. Song, X. Shan, F. Lv, and T. Xie, "A study of vortex-induced energy harvesting from water using PZT piezoelectric cantilever with cylindrical extension," *Ceram. Int.* **41**, S768–S773 (2015).
- M. M. Bernitsas, K. Raghavan, Y. Ben-Simon, and E. Garcia, "VIVACE (vortex induced vibration aquatic clean energy): A new concept in generation of clean and renewable energy from fluid flow," *J. Offshore Mech. Arct. Eng.* **130**, 041101 (2008).
- Y. Nishi, K. Fukuda, and W. Shinohara, "Experimental energy harvesting from fluid flow by using two vibrating masses," *J. Sound Vib.* **394**, 321–332 (2017).
- Z. L. Wang, "Triboelectric nanogenerators as new energy technology for self-powered systems and as active mechanical and chemical sensors," *ACS Nano* **7**, 9533–9557 (2013).
- Y. Wang, H. Wu, L. Xu, H. Zhang, Y. Yang, and Z. L. Wang, "Hierarchically patterned self-powered sensors for multifunctional tactile sensing," *Sci. Adv.* **6**, eabb9083 (2020).
- S. Hao, J. Jiao, Y. Chen, Z. L. Wang, and X. Cao, "Natural wood-based triboelectric nanogenerator as self-powered sensing for smart homes and floors," *Nano Energy* **75**, 104957 (2020).



- <sup>25</sup>P. Bai, G. Zhu, Y. Liu, J. Chen, Q. Jing, W. Yang, J. Ma, G. Zhang, and Z. L. Wang, "Cylindrical rotating triboelectric nanogenerator," *ACS Nano* **7**, 6361–6366 (2013).
- <sup>26</sup>X. Yang, S. Chan, L. Wang, and W. A. Daoud, "Water tank triboelectric nanogenerator for efficient harvesting of water wave energy over a broad frequency range," *Nano Energy* **44**, 388–398 (2018).
- <sup>27</sup>J. Liu, L. Zhou, Y. Gao, P. Yang, D. Liu, W. Qiao, B. Zhang, Z. Zhao, Z. L. Wang, and J. Wang, "Achieving ultra-high voltage (10 kV) triboelectric nanogenerators," *Adv. Energy Mater.* **13**, 2300410 (2023).
- <sup>28</sup>I.-Y. Suh, Z.-Y. Huo, J.-H. Jung, D. Kang, D.-M. Lee, Y.-J. Kim, B. Kim, J. Jeon, P. Zhao, J. Shin *et al.*, "Highly efficient microbial inactivation enabled by tunneling charges injected through two-dimensional electronics," *Sci. Adv.* **10**, ead15067 (2024).
- <sup>29</sup>Z. Zhou, L. Weng, T. Tat, A. Libanori, Z. Lin, L. Ge, J. Yang, and J. Chen, "Smart insole for robust wearable biomechanical energy harvesting in harsh environments," *ACS Nano* **14**, 14126–14133 (2020).
- <sup>30</sup>A. Rayegani, M. Saberian, Z. Delshad, J. Liang, M. Sadiq, A. M. Nazar, S. A. H. Mohsan, and M. A. Khan, "Recent advances in self-powered wearable sensors based on piezoelectric and triboelectric nanogenerators," *Biosensors* **13**, 37 (2022).
- <sup>31</sup>Q. Jiang, Y. Han, W. Tang, H. Zhu, C. Gao, S. Chen, M. Willander, X. Cao, and Z. L. Wang, "Self-powered seawater desalination and electrolysis using flowing kinetic energy," *Nano Energy* **15**, 266–274 (2015).
- <sup>32</sup>D. Zhang, J. Shi, Y. Si, and T. Li, "Multi-grating triboelectric nanogenerator for harvesting low-frequency ocean wave energy," *Nano Energy* **61**, 132–140 (2019).
- <sup>33</sup>D. Guan, G. Xu, X. Xia, J. Wang, and Y. Zi, "Boosting the output performance of the triboelectric nanogenerator through the nonlinear oscillator," *ACS Appl. Mater. Interfaces* **13**, 6331–6338 (2021).
- <sup>34</sup>R. Govardhan and C. Williamson, "Defining the 'modified griffin plot' in vortex-induced vibration: Revealing the effect of Reynolds number using controlled damping," *J. Fluid Mech.* **561**, 147–180 (2006).
- <sup>35</sup>T. Sarpkaya, "A critical review of the intrinsic nature of vortex-induced vibrations," *J. Fluids Struct.* **19**, 389–447 (2004).
- <sup>36</sup>C. H. Williamson and R. Govardhan, "Vortex-induced vibrations," *Annu. Rev. Fluid Mech.* **36**, 413–455 (2004).
- <sup>37</sup>S. Niu, Y. Liu, X. Chen, S. Wang, Y. S. Zhou, L. Lin, Y. Xie, and Z. L. Wang, "Theory of freestanding triboelectric-layer-based nanogenerators," *Nano Energy* **12**, 760–774 (2015).
- <sup>38</sup>M. D. Hussain, B. Dudem, D. I. Kutsarov, and S. R. P. Silva, "Exploring charge regeneration effect in interdigitated array electrodes-based TENGs for a more than 100-fold enhanced power density," *Nano Energy* **130**, 110112 (2024).
- <sup>39</sup>M. T. Rahman, S. S. Rana, M. Salauddin, P. Maharjan, T. Bhatta, H. Kim, H. Cho, and J. Y. Park, "A highly miniaturized freestanding kinetic-impact-based non-resonant hybridized electromagnetic-triboelectric nanogenerator for human induced vibrations harvesting," *Appl. Energy* **279**, 115799 (2020).
- <sup>40</sup>D. Davies, "Charge generation on dielectric surfaces," *J. Phys. D* **2**, 1533 (1969).
- <sup>41</sup>Y. Zi, S. Niu, J. Wang, Z. Wen, W. Tang, and Z. L. Wang, "Standards and figure-of-merits for quantifying the performance of triboelectric nanogenerators," *Nat. Commun.* **6**, 8376 (2015).